cooperates with other agents to come to a consistent overall image segmentation. However, the complexity of this system may lead to time delays when there is a conflict among the agents.

Tuceryan[12] proposed a method for obtaining texture features directly from gray-level images by computing the moments of the image in local regions. The results of his segmentation algorithm show that the image moments computed over local regions provide a powerful set of features that reflect certain textural properties in images.

In this article, as in those by Brusseau et al.[7] and Bovenkamp et al.,[8] we propose a system for automatic luminal contour segmentation. Unlike the Brusseau et al. system,[7] our system is applied to images obtained from a rotating IVUS system because these systems are widely used in clinical settings. Instead of a multiagent system, as proposed by Bovenkamp et al.,[8] we used the simpler and more powerful set of features proposed by Tuceryan[12] to achieve our goal of luminal contour segmentation.

Our strategy to achieve this goal is to extract local moment-based texture features and a pixel position feature from IVUS images to perform a clustering on the basis of these features. Once we obtain the clustered image, a smoothing filter is applied to reduce the irregularities.

Materials and methods

Local moments have attracted attention as local features in applications such as edge detection and texture segmentation.[13-18] The main reason for this is that they are inherently integral-based features, so their use reduces the effect of uncorrelated noise. The computation of local moments, when viewed as a neighborhood operation, can be interpreted as a convolution of the image with a set of masks.[12] Tuceryan successfully proved the efficacy of local moments in texture segmentation.[12] However, in the case of luminal contour detection in IVUS images, an additional feature was necessary to take into account the concentric circular arrangement of artery layers. The feature used to carry this out was the radial distance.

Our texture segmentation algorithm is based on Tuceryan's work[12] and consists of the following steps:

Step 1: Compute the image moments within a small window around each pixel.

Step 2: Compute the texture features from the moments by applying a nonlinear transformation followed by an averaging operation.

Step 3: Compute the radial distance.

Step 4: For each pixel in the input image, compose a feature vector formed by features computed in step 2 and the radial distance computed in step 3.

Step 5: Perform a fuzzy clustering of the input image pixels on the basis of their feature vectors.

Step 6: Classify every pixel in the input image according to the minimum distance from the center of the clusters found in step 5.

Step 7: Perform morphological contour smoothing on the segmented image found in step 6.

Step 8: Find the final lumen contour by applying the Sobel operator[19] to the contour-smoothed image obtained in step 7.

Moments

Our algorithm uses the moments of an image to compute texture features. The $(p + q)$-th order moment m_{pq} of a function of two variables $f(x,y)$ with respect to the origin $(0,0)$ is defined as[12]:

$$m_{pq} = \int_{-\infty}^{\infty} \int_{-\infty}^{\infty} f(x,y)x^p y^q dx dy \qquad (1)$$

where $p,q = 0,1,2,\ldots$. Normally, the moments are computed over some bounded region. If the function is equal to unity within the region and zero outside the region, the lower order moments (small values of p and q) have well-defined interpretations. For example, m_{00} is the area of the region, m_{10}/m_{00} and m_{01}/m_{00}, giving the x and y coordinates of the centroid for the region, respectively. The m_{20}, m_{11}, and m_{02} can be used to derive the amount of elongation of the region and the orientation of its major axis. The higher-order moments give even more detailed shape characteristics of the polygons such as symmetry.

In this article, as in Tuceryan's work,[12] we regard the intensity image as a function of two variables, $f(x,y)$. We compute a fixed number of the lower-order moments for each pixel in the image (we use $p + q \leq 2$). The moments are computed within a small local window around each pixel. Given a window size W, the coordinates are normalized to the range of $[-0.5, 0.5]$ and the pixel is located at the center. The moments are computed with respect to this normalized coordinate system, which permits us to compare the set of moments computed for each pixel. We always choose the window width W to be odd so that the pixel (i,j) is centered on a grid point.

Let (i,j) be the pixel coordinates for which the moments are computed. For a pixel with coordinates (k, l) that falls within the window, the normalized coordinates (x_k, y_l) are given by:
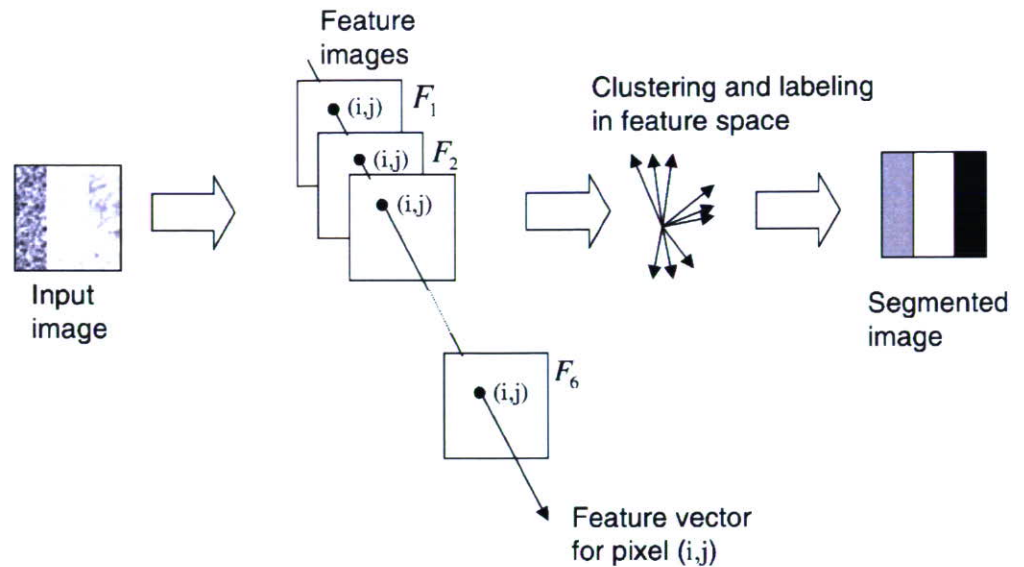
$$x_k = \frac{k-i}{W} \qquad y_l = \frac{l-j}{W} \qquad (2)$$

Then the moment $m_{pq}(i,j)$ within a window centered at pixel (i,j) is computed by a discrete sum approximation of Eq. 1 that uses the normalized coordinates (x_k, y_l):

$$m_{pq}(i,j) = \sum_{k=-W/2}^{W/2} \sum_{l=-W/2}^{W/2} f(i+k, j+l)x_k^p y_l^q \qquad (3)$$

This discrete computation of the set of moments for a given pixel over a finite rectangular window corresponds to a neighborhood operation, and, therefore, it can be interpreted as a convolution of the image with a mask.[12]

Feature images

F_1 (i,j)

F_2 (i,j)

(i,j)

Input image

Clustering and labeling in feature space

Segmented image

F_6 (i,j)

Feature vector for pixel (i,j)

When we examine these masks, we see that they can be interpreted as local feature detectors. For example, the mask for m_{00} corresponds to a box-averaging window, and thus it can be interpreted as computing the total energy within that box. The masks for m_{10} and m_{01} take the form of edge detectors. They would respond to sudden intensity changes in the x and y directions, respectively. The second-order moments are not easy to interpret; the only exception being m_{11}, which looks like a cross detector.[12]

The set of values for each moment over the entire image can be regarded as a feature image. Let M_k be the k-th such image. If we use n moments, then there will be n such moment images. In our experiments, we used up to second-order moments. That is, we used m_{00}, m_{01}, m_{10}, m_{11}, m_{02}, and m_{20}, which result in the images M_1, M_2, M_3, M_4, M_5, and M_6, respectively.

To enhance the discrimination power of these moments, we adopted the transformation used by Tuceryan.[12] Then, we introduced a nonlinear transducer that maps moments to texture features.

Thus, we obtain the texture feature image F_k corresponding to the moment image M_k with mean $\overline{M}$ using the following transformation:

$$F_k(i,j) = \frac{1}{L^2} \sum_{(a,b)\in\omega_{ij}} \left|\tanh\left(\sigma\left(M_k(a,b) - \overline{M}_k\right)\right)\right|; \qquad k = 1,2,\ldots,6$$

(4)

where ω_{ij} is an $L \times L$ averaging window centered at location (i, j) and σ controls the shape of the function (we used $\sigma = 0.01$). Figure 1 shows a graphic representation of a segmentation process on the basis of the feature images.

The window size depends on the content of the image: finer textures require a smaller window size to detect smaller features, whereas coarser textures require a larger window. The parameters σ (in Eq. 4), moment window size W, and average window size L were chosen by gradually adjusting these values and observing the resultant effect in the segmented images. Initially, tests were done with increasing values of L for a fixed value W. Then, the fixed value W was increased and tested with increasing values of L. This process was repeated using the values 5, 7, 9, and 11 for W and L. Window sizes less than 5 were insufficient to capture the texture information, and sizes greater than 11 may lead to error in the contour definition. The choice of the best combination of values for W and L was based on visual evaluation of the resultant segmented images. After that, an adjustment of the parameter σ was made starting with the suggested[12] value 0.01. The range from 0.01 to 0.05 offered good results. The final chosen values were $W = 7$, $L = 9$, and $\sigma = 0.01$. They were determined empirically and are probably not optimal.

Luminal contour definition

The problem of luminal contour definition can be regarded as a clustering problem whose main point is to find features to each pixel of the IVUS image that could permit an accurate clustering and then to obtain a segmentation of regions of interest for physiologists such as the lumen, for example.

Due to the encouraging results obtained by Tuceryan,[12] the theory of moment-based texture segmentation was applied to the problem of luminal contour detection in IVUS images. The system proposed in this article can be represented in the block diagram shown in Fig. 2. The motivation for implementing this procedure for detection of the lumen boundary is that the IVUS images usually have very smooth gray-level transition between their regions and also there is noise. These facts make it difficult to detect the contour of the lumen region using only the traditional methods of edge detection such as Sobel and Canny operators[19,20] directly. An example is shown in Fig. 3. Thus, in the proposed system we identify the pixels that belong to the

Fig. 2. Block diagram of the proposed system for luminal contour segmentation
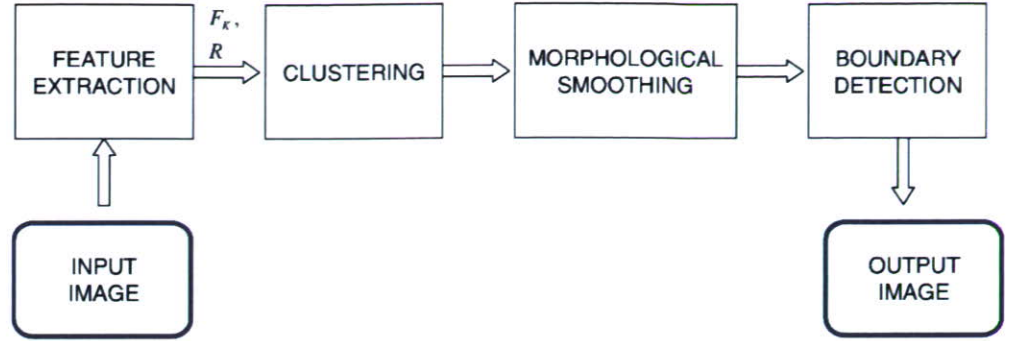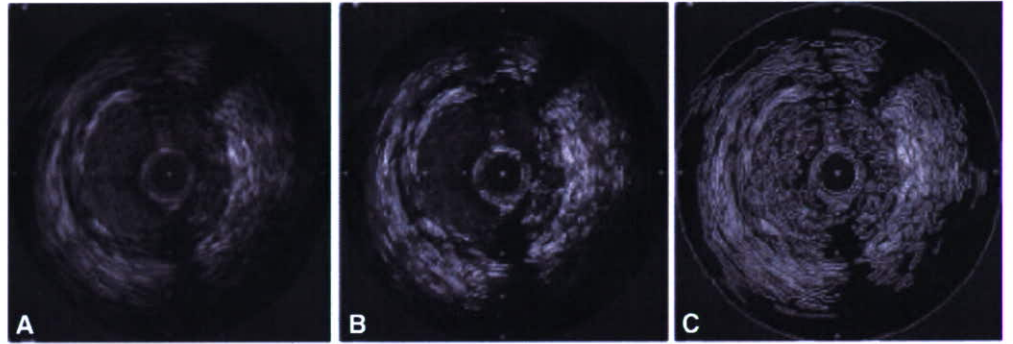

Fig. 3. Application of edge detection methods. **A** Original image. **B** Result of application of Sobel operator. **C** Result of application of Canny operator

lumen region through clustering based on their texture features and radial position feature. Then, we obtain images with regions well defined. After that we can easily detect the lumen contour using the traditional edge detection techniques.

Input image

In the proposed system (see Fig. 2), the input image is the original image obtained from the IVUS system. In this work, we used a commercially available IVUS system (Clear View Ultra; Boston Scientific, Natick, MA, USA). The central frequency of the rotating IVUS probe (Atlantis SR Pro; Boston Scientific) was 40MHz.

Feature extraction

The feature extraction block is in charge of extraction of the transformed versions of the moments, F_k ; $k = 1, 2, \ldots, 6$, already defined, and the radial distance R is presented graphically in Fig. 4.

Examples of the moment images are shown in Fig. 5. Some vertical and horizontal elongated textures became slightly enhanced in the lumen region, especially in images M_4, M_2, and M_3, and more weakly in images M_5 and M_6. Image M_1 is a blurred version of the original image giving information about the average gray level. After application
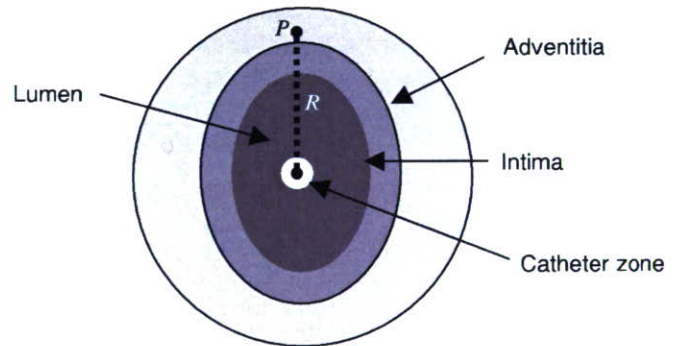

Fig. 4. Illustration of a cross section of a blood vessel. R, radial distance; P, pixel

of the nonlinear transformation (Eq. 4), these images became enhanced (Fig. 6). The lumen region became differentiated from the other regions, except in image F_1 that slightly enhanced the edges by computing the average gray level.

However, even after applying nonlinear transformation, these features were not sufficient to lead to reasonable lumen region segmentation. Then, the radial distance feature R was added to the clustering process.

In this work, we define the radial distance R as the distance from the central pixel of the image to the position of the pixel P under consideration. This distance R is normalized and becomes the seventh feature used in the following clustering of the input image pixels. The radial distance R is
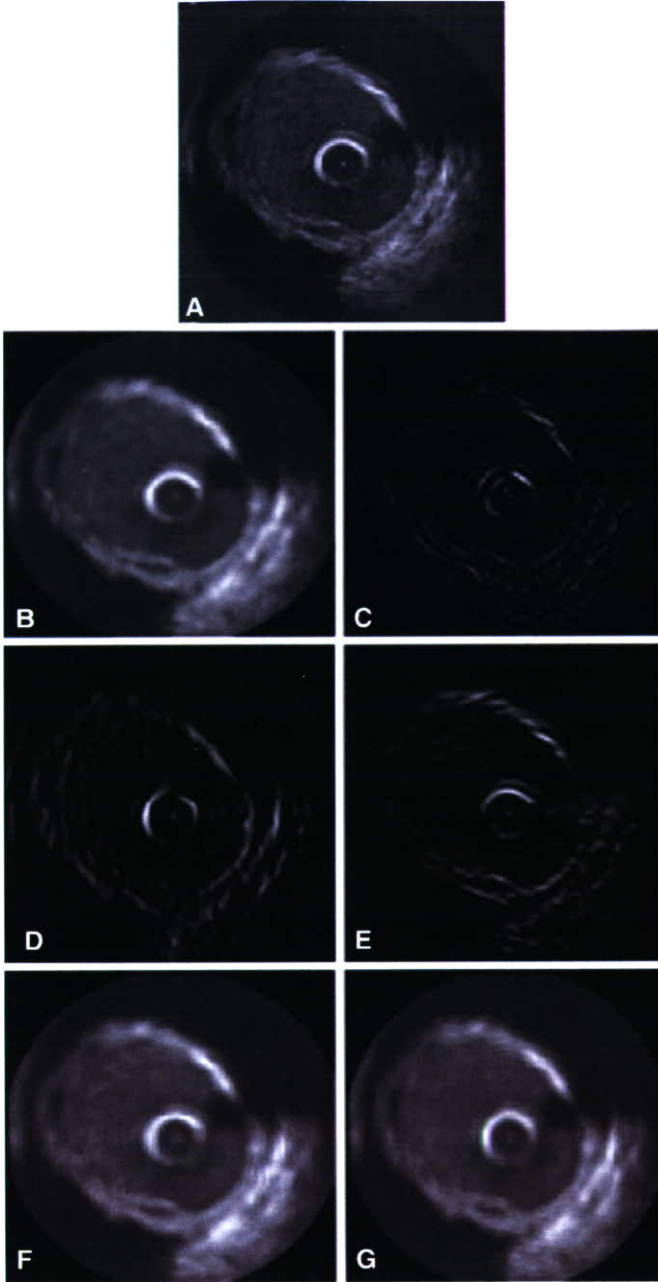
Fig. 5. Moment images. **A** Original image. **B** Moment image M_1. **C** Moment image M_4. **D** Moment image M_2. **E** Moment image M_3. **F** Moment image M_5. **G** Moment image M_6

Fig. 6. Feature images. **A** Original image. **B** Final segmented image. **C** Feature image F_1. **D** Feature image F_4. **E** Feature image F_2. **F** Feature image F_3. **G** Feature image F_5. **H** Feature image F_6

of fundamental importance because it allows pixels that are at similar distance from the center of the image to be included in the same cluster if they have similar texture features. The effect of the use of these texture and position features is that the clusters become organized in regions similar to concentric rings around the center pixel; this is associated with the physiological structure of the blood vessels, as represented in Fig. 4. The effect of adding the radial distance feature R to the feature vector can be observed in Fig. 7. Thus, these seven features were used to comprise a feature vector for each pixel of the image.
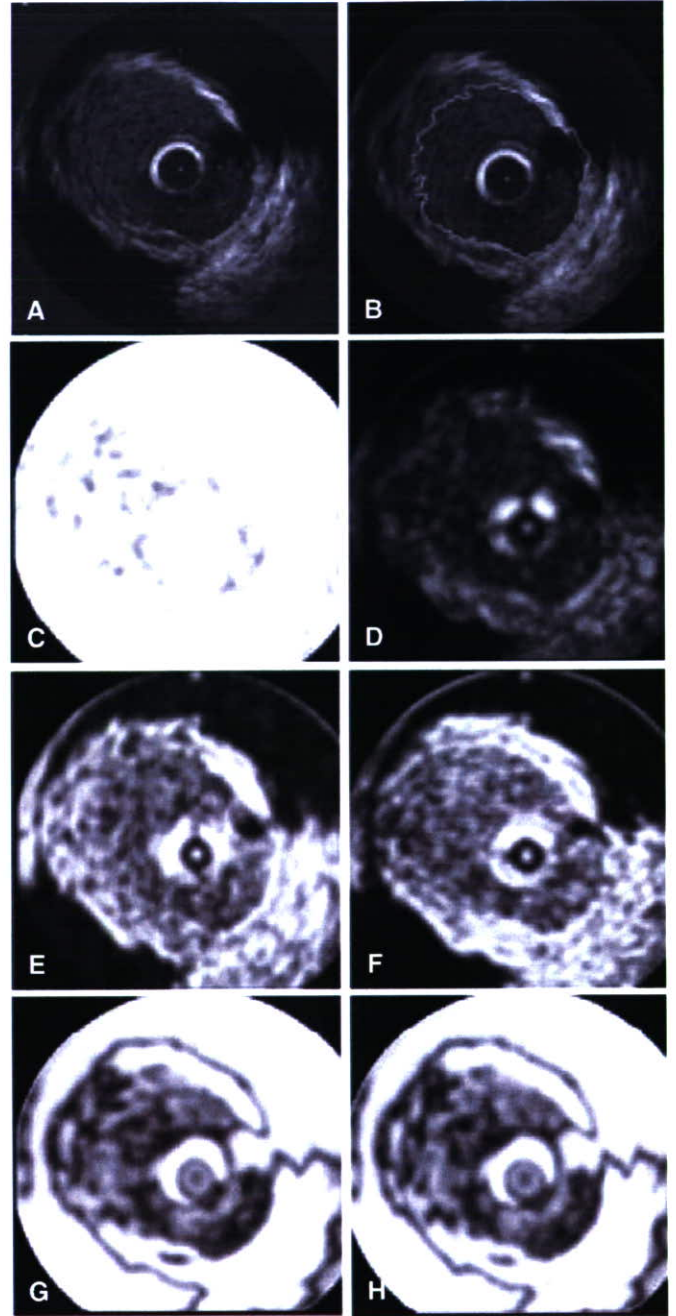
Clustering

In this block we used the well-known Fuzzy C-Means[21] algorithm, which has been successfully utilized in several image processing applications in the field of medical imaging.[22] This clustering technique uses the feature vectors to distinguish the different regions of the image. Through successive iterations of an optimization routine, the central vector of each cluster is found. Then, the input image pixels are assigned to the cluster whose center vector is the closest to their feature vector. The number of clusters chosen was

Fig. 7. Effect of the radial position feature R as one of the components of the feature vector. **A** and **B** are the same images obtained from patient A. **A** Clustered image without using the radial distance feature R. **B** Clustered image using the radial distance feature R
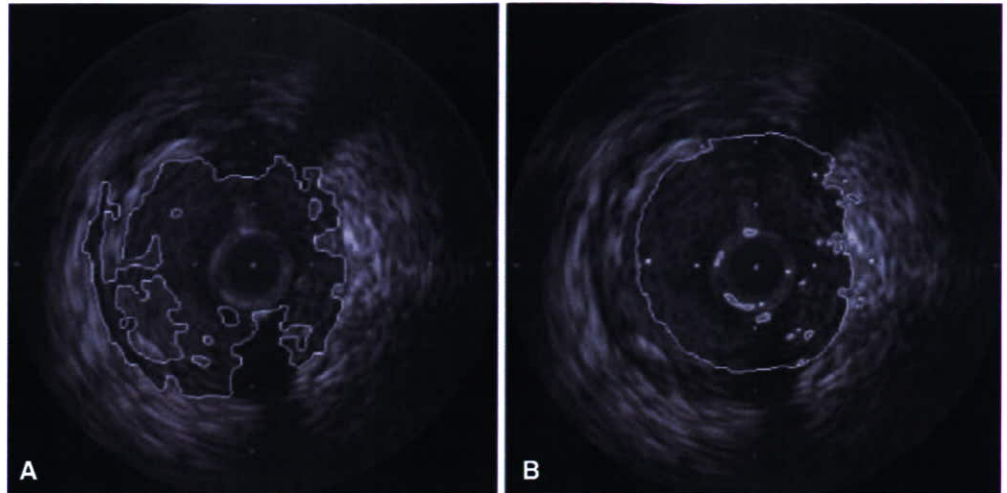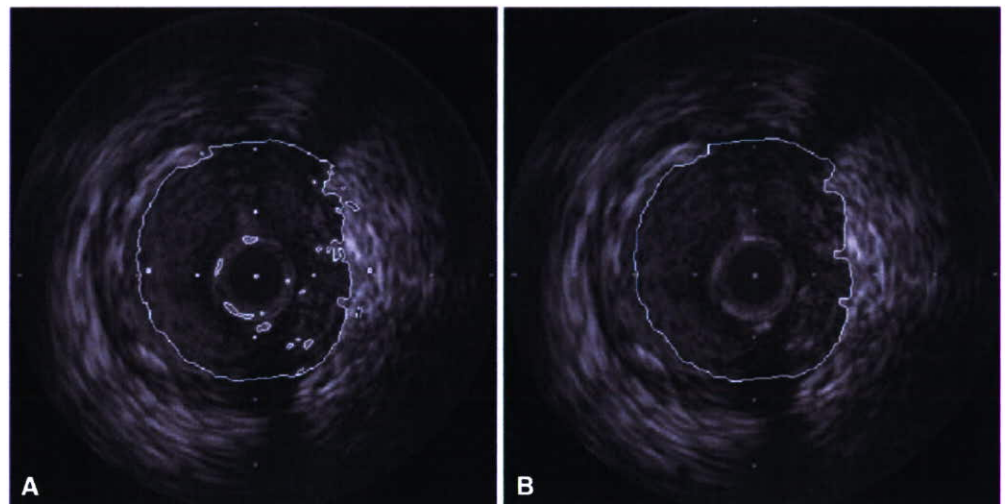

Fig. 8. A Result of clustering. **B** Result of morphological filtering

four: one cluster for the external region, one for the region between the adventitia and intima, one for the lumen, and another one for the catheter zone.

Morphological smoothing

Mathematical morphology is a technique of image processing whose value for each pixel in the output image is based on a comparison of the corresponding pixel in the input image with its neighbors. By choosing the size and shape of the neighborhood, we can define a morphological operation that is sensitive to specific shapes in the input image. The neighborhood size and shape are determined by the size and shape of a second, usually much smaller, image called a *structuring element*, which together with the input image is regarded as a set. Thus, basic operations of set theory, such as union, subtraction, and complement can be carried out with both images. These basic operations can be used to compose other operations, such as *opening* and *closing*.

Opening generally smoothes the contour of an object, breaks narrow isthmuses, and eliminates thin protrusions. Closing also tends to smooth sections of contour, but, as opposed to opening, it generally fuses narrow breaks and long thin gulfs, eliminates small holes, and fills gaps in the contour.[19]

To reduce the irregularities of the borders as well as some small regions around the borders, morphological filtering is done before boundary detection. This filtering is performed through the application of opening and closing morphological operations with a disk-structuring element of size 3. An example of the result of the luminal contour obtained only with the clustering process without any contour smoothing can be seen in Fig. 8A. An example of the luminal contour obtained when a morphological filter is applied after the clustering and before the boundary detection process is shown in Fig. 8B. Comparing these figures, we can observe that the morphological filter reduced the irregularities in the segmented contour and eliminated the small segmented regions.

Fig. 9. Example of luminal
contour detection. **A** and **B** are
the same images obtained from
patient A. **A** Automatically
defined luminal contour.
B Manually defined luminal
contour. **C** and **D** are the same
images obtained from patient B.
C Automatically defined luminal
contour. **D** Manually defined
luminal contour
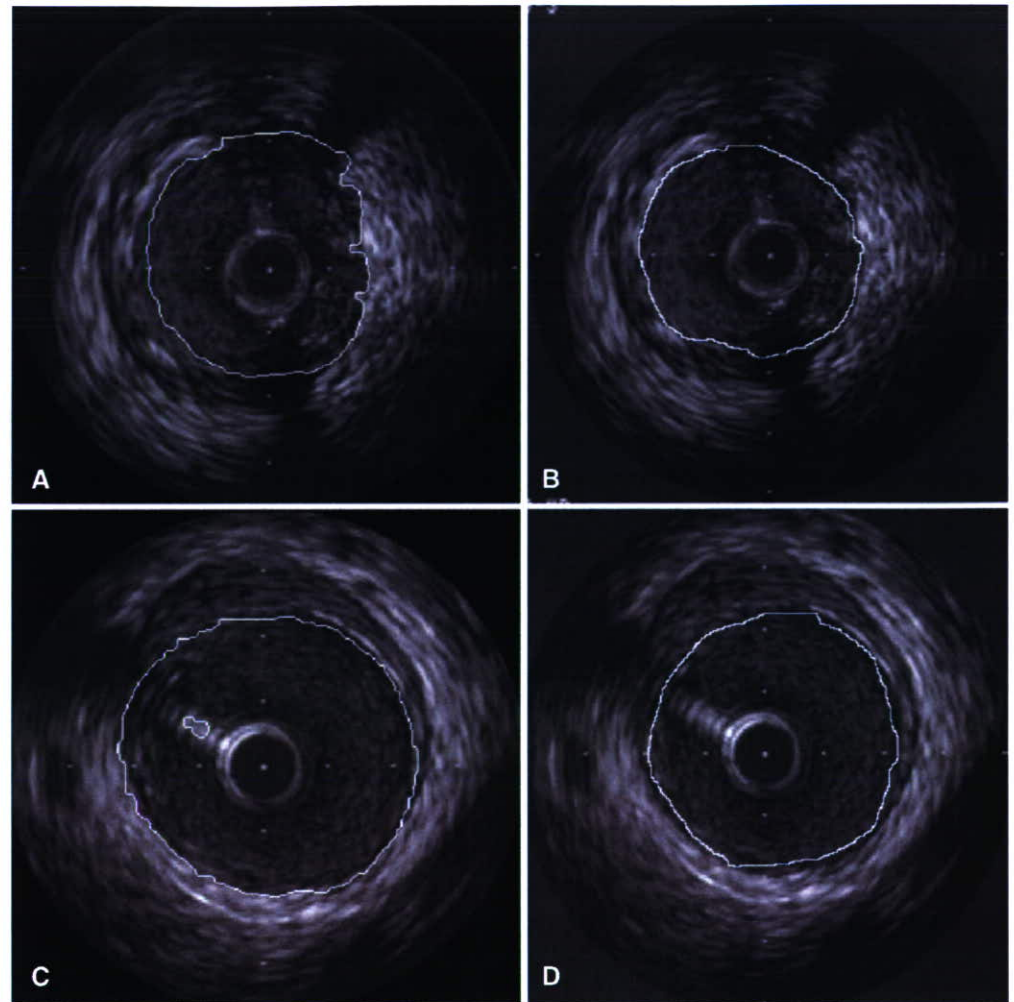
Boundary detection

After the clustering and contour smoothing, the images had
well-defined regions, with contours that could easily be
detected by traditional edge detection methods. In this
system, we used the Sobel operator[19] because of its sim-
plicity and efficiency. The Sobel operator performs a two-
dimensional (2-D) spatial gradient measurement on an
image, thereby emphasizing the regions of abrupt changes
in gray level that correspond to edges.

Results

Using the system presented above, tests were done with 15
IVUS images of different patients. Cases with totally occlu-
sive plaque and large shadow regions were not considered.
Some examples of the results are shown in Fig. 9 together
with the corresponding images that were segmented by a
medical doctor for comparison.

We can see that the boundaries automatically drawn by
the proposed system closely resemble those drawn manu-
ally by a medical doctor. However, some errors can be

observed in the dark regions, in general caused by shadows
that follow hard plaque or due to the guidewire. In these
regions, the system tends to segment a region larger than
that which would be segmented by a medical doctor; this
occurs mainly because these dark regions contain no texture
information and lead the system to be segment based only
on the radial distance information. Thus, in the dark regions,
the system tends to draw lines sometimes quite different
from those drawn by a medical doctor (Fig. 10).

Sometimes bright regions appeared around the catheter
zone, leading to a catheter cluster larger than the normal.
However, as the size and position of the catheter are quite
predictable, we can easily eliminate this effect in most of the
images by compensating for the catheter cluster area.

The correlation between the areas of the automatically
defined lumen and manually defined lumen is shown in Fig.
11. The correlation coefficient was equal to 0.86.

Discussion

The transition between the lumen and the vessel wall, as
well as the transition between the vessel layers, is quite

Fig. 10. Example of influence of guidewire shadow on the luminal contour detection process. **A** and **B** are the same images obtained from patient C. **A** Automatically defined luminal contour. **B** Manually defined luminal contour
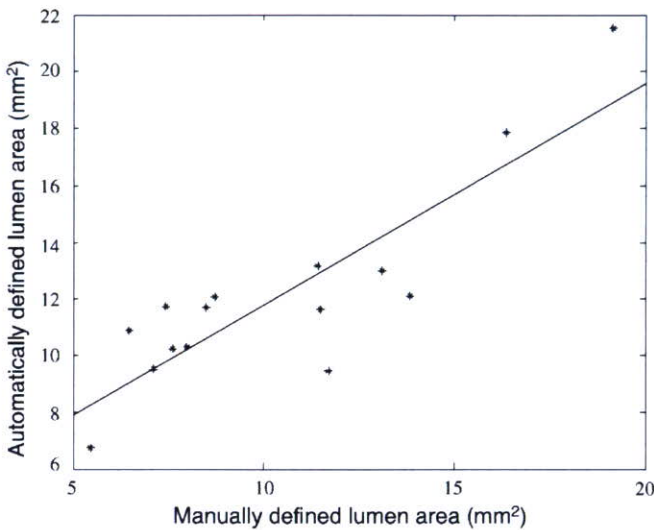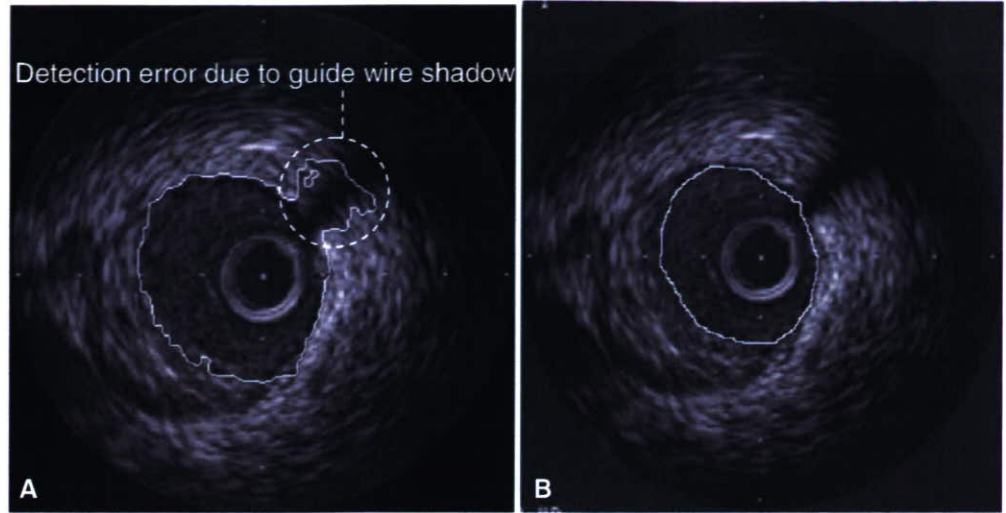

Fig. 11. Correspondence between lumen area manually defined and the same area automatically defined

smooth, making boundary detection based on local features a hard task. However, due to the ability of the local moment in distinguishing textured regions together with the radial distance, which is usually small in the lumen region, it was possible to overcome the difficulty caused by the smooth transition between regions. We can see that the automatically segmented image presented in Fig. 9A has a better luminal contour definition than the images yielded by the traditional methods presented in Fig. 3. We can also see that the automatically segmented images presented in Fig. 9 closely resemble the images manually segmented.

The effectiveness of the proposed radial distance feature R can be observed in Fig. 7. In Fig. 7A we see an example of segmentation without using the feature R. In this case, the resulting segmentation is more irregular and contains some subregions segmented inside the lumen region. This oversegmentation occurs mainly because of some texture and gray-level changes inside the lumen region. When the radial distance feature R is added to the clustering process, the differences among these segmented subregions is overcome because they acquire a feature that is similar in most of them, and then this strongly influences the clustering result. Thus, we can obtain a more regular and compact segmentation of the lumen region as shown in Fig. 7B.

In our tests, the moment-based texture features alone could not provide sufficient information for reasonably accurate lumen segmentation. The original contribution of this work is the combination of moment-based texture features with a position feature to comprise feature vectors for the clustering of IVUS images leading to reasonable segmentation of luminal contour.

However, the outer boundary of the vessel was not accurately detected, mainly because of the much smoother transition between the vessel external wall and the surrounding tissues. To overcome this difficulty, it seems that more global features need to be added to the system.

The problem of the error shown in Fig. 10A that is generated by the guidewire and shadowed area seems hard to solve using only these features based on moment and the radial distance because actually these regions contain no texture information. Thus, it seems that some kind of high-level knowledge needs to be introduced in the system to mimic human reasoning, as has recently been proposed by Bovenkamp with the multiagent system.[8] Another possibility is a previous elimination of the region shadowed by the guidewire from the image to be processed and, at the end, to make an interpolation to close the boundary found automatically.

Morphological smoothing could reduce the irregularities present in the detected contour. This technique proved to be useful in this application because it could efficiently eliminate the small unwanted segmented regions.

Luminal contour definition is also very useful in the process of plaque segmentation, as has been commented in a previous work.[23] The lumen boundary can be used to refine the space of search for plaque in an IVUS image

because the plaque always appears inside the walls of the vessel. Thus, the luminal contour can be used as an inner border of a region of search for plaque.

The delimitation of a region of search for plaque is especially important for systems whose identification method is based on clustering techniques and histograms. Elimination of the lumen region from the process of clustering also solves the problem of ring-down artifacts in the catheter zone that frequently appear as bright regions in IVUS images and sometimes influences the plaque segmentation process.

The window sizes depend on the content of the image: finer textures require a smaller window size to detect smaller features and coarser textures require larger windows. Thus, as the texture of the lumen region is finer than vessel wall texture, an adaptive method for adjustment of window size would probably be useful in the detection of the vessel contour.

Conclusions

In this article, an automatic algorithm dedicated to luminal contour segmentation in IVUS images has been introduced. This technique performs clustering of an input image on the basis of moment-based texture features and the radial distance.

Based on our tests, we can conclude that the moment-based texture features together with radial distance are feasible components for a feature vector in IVUS image segmentation when the aim is to find the luminal contour. However, some errors still occurred in the regions with shadows.

The process was improved when a morphological smoothing filtering was carried out after the clustering and before the boundary detection process. Tests performed with 15 images from different patients resulted in a correlation coefficient of 0.86 between the lumen areas automatically detected and the lumen areas manually detected.

Only the segmentation of the luminal contour has been considered. As future work, we plan to extend this method to detection of the vessel contour, which is necessary for assessment of the degree of vessel stenosis. In practical terms, once having determined the position of the blood-tissue interface, the luminal area will be excluded and the second contour will be searched in the remaining region.

References

1. Zhang X, Charles R, Sonka M. Tissue characterization in intravascular ultrasound images. IEEE Trans Med Imaging 1998;17:889–99.
2. Vince D, Dixon K, Cothren R, Cornhill J. Comparison of texture analysis methods for characterization of coronary plaques in intravascular ultrasound images. Comput Med Imaging Graphics 2000;24:221–9.
3. Solaiman B, Debon R, Pipelier F, et al. Information fusion: application to data and model fusion for ultrasound image segmentation. IEEE Trans BiomedEng 1999;46:1171–5.
4. Sonka M, Zhang X, Siebes M, et al. Segmentation of intravascular ultrasound images: a knowledge-based approach. IEEE Trans Med Imaging 1995;14:719–32.
5. Gronningsaeter A, Bjorn A, Heimdal A, et al. Vessel wall detection and blood noise reduction in intravascular ultrasound imaging. IEEE Trans Ultrasonics Ferroelectrics Freq Control 1996;43: 359–69.
6. Wink O, Niessen W, Viergever M. Fast delineation and visualization of vessels in 3D angiographic images. IEEE Trans Med Imaging 2000;19:337–46.
7. Brusseau E, Korte CL, Mastik F, et al. Fully automatic luminal contour segmentation in intracoronary ultrasound imaging – a statistical approach. IEEE Trans Med Imaging 2004;23:554–66.
8. Bovenkamp EGP, Dijkstra J, Bosch JG, et al. Multi-agent segmentation of IVUS images. Pattern Recog 2004;37:647–63.
9. Shiina T, Nitta N, Ueno E, et al. Real time tissue elasticity imaging using the combined autocorrelation method. J Med Ultrasonics 2002;29:119–28.
10. Ophir S, Alam SK, Garra BS, et al. Elastography: imaging the elastic properties of soft tissues with ultrasound. J Med Ultrasonics 2002;29:155–71.
11. Wang Y, Itoh K, Taniguchi N, et al. Studies on tissue characterization by texture analysis with co-occurrence matrix method using ultrasonography and CT Imaging. J Med Ultrasonics 2002;29: 211–23.
12. Tuceryan M. Moment based texture segmentation. Proceedings of 11th IAPR International Conference on Image, Speech, Signal Analysis and Pattern Recognition 1992:45–8.
13. The CH, Chin RT. On image analysis by methods of moments. IEEE Trans Pattern Anal Machine Intelligence 1988;10:496–513.
14. Khotanzad A, Hong YH. Invariant image recognition by Zernike moments. IEEE TransPattern Anal Machine Intelligence 1990;12: 489–97.
15. Martinez J, Thomas F. Efficient computation of local geometric moments. IEEE Trans Image Processing 2002;11:1102–11.
16. Sheynin S, Tuzikov A. Moment computation for objects with spline curve boundary. IEEE Trans Pattern AnalMachine Intelligence 2003;25:1317–22.
17. Yap P, Paramesran R. Image analysis by Krawtchouk moments. IEEE Trans Image Processing 2003;12:1367–77.
18. Suhling M, Arigovindan M, Hunziker P. Multiresolution moment filters: theory and applications. IEEE Trans Image Processing 2004;13:484–95.
19. Gonzales RC, Woods RE. In: Digital image processing. 2nd ed. New Jersey: Prentice Hall; 2002. p. 519–80.
20. Canny J. A computational approach to edge detection. IEEE Trans Pattern Anal Machine Intelligence 1986;8:679–98.
21. Bezdek JC. In: Pattern recognition with fuzzy objective function algorithms. New York: Plenum Press; 1981. p. 65–85.
22. Masulli F, Schenone A. A fuzzy clustering based segmentation system as support to diagnosis in medical imaging. Artif Intell Med 1999;16:129–47.
23. Santos Filho E, Yoshizawa M, Tanaka A, et al. An adaptive fuzzy segmentation of intravascular ultrasound images. Proc IEEE Int Symp Biomed Imaging 2004:1311–4.

Ultrasonic Tissue Characterization of Photodamaged Skin by Scanning Acoustic Microscopy

Muneo MIYASAKA, Shingo SAKAI*, Ayumi KUSAKA*, Yoko ENDO*,
Masaki KOBAYASHI*, Kazuto KOBAYASHI**,
Naohiro HOZUMI*** and Ryuzaburo TANINO

Department of Plastic Surgery, Tokai University School of Medicine
*Basic Research Laboratory, Kanebo Cosmetics Inc.,
**Research & Development Dept., Honda Electronics Co., Ltd.,
***Dept. of Electrical & Electronic Engineering, Toyohashi University of Technology

The aim of this study was to ultrasonically characterize photodamaged skin of the elderly at the microscopic level using scanning acoustic microscopy which showed two-dimentional distribution of sound speed in the skin section. We confirmed that the expression level of the elastin gene was increased in the preauricular skin (photodamaged area), compared with postauricular skin (photo-protected area). The expression level of the procollagen gene was also increased in the preauricular skin compared with postauricular skin. The preauricular skin showed higher sound speed in the papillary dermis (Grenz zone). The site of progressive solar elastosis showed a somewhat sound speed velocity than that of the Grenz zone. Immunohistochemical staining showed conserved deposition of collagen in the Grenz zone even in the more photodamaged preauricular skin. These results suggest that fibrosis in the Grenz zone compensates tissue strength with the progress of solar elastosis. The sound speed analysis of skin will provide important information on heterogeneous mechanical changes in the skin during the process of photoaging.

Key words: ultrasound, scanning acoustic microscopy, sound speed, collagen, photoaging, papillary dermis

Abbreviations: SC, stratum corneum; SAM, scanning acoustic microscope; EVG stain, elastica van Gieson's stain; MMP, matrix metalloproteinase.

INTRODUCTION

Photoaging is distinguished from intrinsic aging and shows some distinctive histological alterations including enlargement and dysplasia of keratinocytes in the epidermis, solar elastosis and a mixed inflammatory infiltrate in the dermis [1]. In particular, the dermal degeneration such as collagen [2, 3], elastin [4] and basal membrane [5] degeneration cause a decrease in the elasticity of skin [6], and promote the formation of wrinkles. So far, skin elasticity has been measured as a total physical property of multilayers such as the stratum corneum, keratinocyte layer and the dermis. Even in the dermis, there are the differences in thickness of collagen fibers [7] and the direction of elastic fibers [8] from the papillary dermis to the reticular dermis, but the contribution of localized changes in the physical properties of the dermis to the whole-skin elasticity during photoaging remains obscure. It is also important to clarify localized changes of physical properties in the skin in the formation of wrinkles.

A scanning acoustic microscope (SAM) system has been used to determine quantitatively the ultrasonic properties of tissue at the microscopic level. Two-
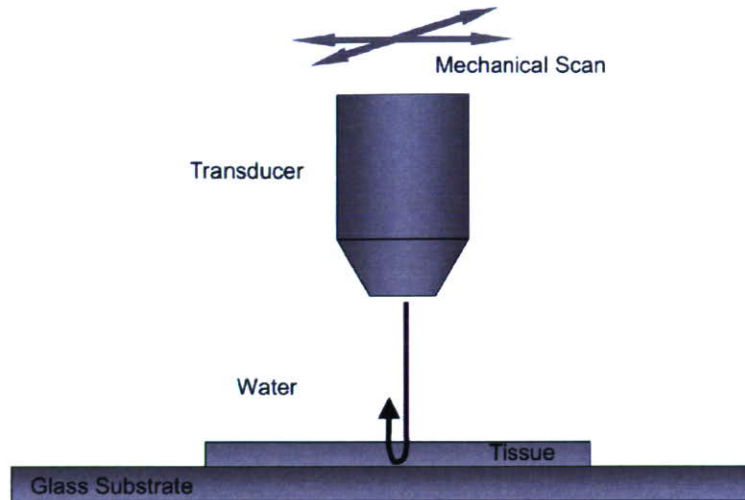
Muneo MIYASAKA, Department of Plastic and Reconstructive Surgery, Tokai University School of Medicine, Bohseidai, Isehara, Kanagawa 259-1193, Japan Tel: +81-463-93-1121 Fax: +81-463-93-7231 E-mail: miyasaka@is.icc.u-tokai.ac.jp

Fig. 1 Concept of ultrasonic microscopy for tissue characterization.

dimensional distribution of sound speed in microscopic sections can be obtained using the SAM system. The sound speed is considered to be mainly determined by the elastic property of tissue components on the assumption that biological tissue is fluid-like. In fact, Verdonk *et al.* [9] and Hoffmeister *et al.* [10] demonstrated that the velocity parallel to myocardial fibers was faster than the velocity perpendicular to the fibers. Saijo *et al.* reported high sound speed in fibrotic sites in the myocordium of patients with myocordial infarction [11]. However, measurement of the distribution of sound speed in the skin tissue using the SAM system has not been widely reported.

In this study, we ultrasonically characterize and compare a photodamaged skin section (preauricular area), and photo-protected skin (postauricular area but not buttock skin) using scanning acoustic microscopy, because regional differences in the structure of the skin have been reported [12].

MATERIALS AND METHODS

Biopsies

Eight Japanese volunteers (three men and five women; age range 66-83 years) were recruited for this study. Surgical biopsies were taken from both the preauricular skin and the postauricular skin of the same subject. The Tokai University Hospital Ethics Committee approved the study, and written consent was obtained from all subjects. Four healthy Caucasian female volunteers (age range 63-69 years) were also recruited. Punch biopsies (3 mm) were taken from the

buttocks of each subject. Informed consent in writing was obtain from all subjects. Biopsy specimens were fixed in formalin, embedded in paraffin, sectioned to 10µm in thickness using a microtome, and deparaffinized for measurement using SAM.

Measurements By Scanning Acoustic Microscopy
Experimental setup

Figure 1 illustrates the concept of the ultrasonic microscope (HUM-1000, Honda Electronics Co., Ltd., Toyohashi, Japan) for tissue characterization. An acoustic wave is transmitted and received by the same transducer. Distilled water is used for the coupling medium between the specimen and the transducer. Reflections at both surfaces of the tissue are compared to measure the sound speed and thickness. Two-dimensional profiles of reflection intensity, thickness and sound speed can be obtained by mechanically scanning the transducer.

The transducer was 1.2 mm in aperture diameter, and 1.5 mm in focal length. Its nominal frequency range was 50-105 MHz (−6 dB), with a central frequency of 80 MHz. An acoustic wave with a wide frequency component was generated by applying the voltage pulse, and irradiated the substrate. The reflection was detected by the same transducer, and was introduced into the analog digital converter (ADC). The band limit and sampling rate were 500 MHz and 2.0 GS/s, respectively. In order to reduce random noise, eight of responses at the same point were averaged in the ADC before being introduced into the computer. The transducer

was mounted on an X-Y stage that was driven by the computer. Considering the focal distance and the cross sectional area of the transducer, the diameter of the focal spot was estimated to be 18µm at 80 MHz.

Analysis

The analysis for the pulse driven type microscopy is illustrated in Fig. 1 in comparison with the conventional burst driven type. The reflected wave is composed of the reflection at the front and rear surfaces of the tissue slice. In the pulse driven type, the reflected wave in the time domain is Fourier transformed into the frequency domain. Then the attenuation and phase spectra are compared with those of the direct reflection at the glass surface where no tissue is present. Because the signal is the result of the interference of two reflections, the attenuation spectrum has both maximum and minimum points as a function of frequency. Assuming f_m as one of the minimum and maximum points, and ϕ_m as the corresponding phase angle, the phase lag between the above two reflections at the minimum point is $(2n-1)\pi$, giving

$$2\pi f_m \times \frac{2d}{c_0} = \phi_m + (2n-1)\pi \tag{1},$$

where d, co, and n are the tissue thickness, sound speed of the water, and a non-negative integer, respectively. The phase lag at the maximum point is $2n\pi$, giving

$$2\pi f_m \times \frac{2d}{c_0} = \phi_m + 2n\pi \tag{2}.$$

The phase angle ϕ_m can be expressed by

$$2\pi f_m \times 2d(\frac{1}{c_0} - \frac{1}{c}) = \phi_m \tag{3},$$

since ϕ_m is the phase lag between the wave passing through distance 2d with sound speed c and that passing though the corresponding distance with sound speed co. From eqs. (1) and (3),

$$d = \{\phi_m + (2n-1)\pi\}c_0/4\pi f_m \tag{4}$$

is obtained. The thickness d can also be obtained from eqs. (2) and (3) as

$$d = \{\phi_m + 2n\pi\}c_0/4\pi f_m \tag{5}.$$

The sound speed is subsequently obtained

as

$$c = (\frac{1}{c_0} - \frac{\phi_m}{4\pi f_m d})^{-1} \tag{6}.$$

After the measurement, staining with elastica van Gieson's stain was performed.

Real-time PCR

The specimens for total RNA extraction were conserved in RNAlater (Ambion, Austin, TX). Total RNA was isolated from human skin samples using TRIzol reagent (Invitrogen Life Technologies, Carlsbad, CA) and RNeasy Mini Kit (Qiagen, Valencia, CA). cDNA synthesis was carried out with MessageSensor™ RT Kit (Ambion). Real-time PCR was performed on the ABI PRISM 7000 Sequence Detection System (Applied Biosystems, Foster City, CA) using TaqMan Gene Expression probes and TaqMan Universal PCR Master Mix (Applied Biosystems). Gene-specific primers (Assay ID) were as follows: Type I collagen $a1$ subunit (COL1A1), Hs00164004; Type I collagen $a2$ subunit (COL1A2), Hs00164099; and tropoelastin (ELN), Hs00355783. The quantity of PCR products was calculated from the cycle threshold value. The levels of gene expression were normalized with those of the GAPDH gene.

Statistical analysis was performed using the Wilcoxon signed-rank test.

Immunohistochemical staining

Paraffin-embedded biopsies were sectioned (5µm), deparaffinized, ethanol-rehydrated, subjected to antigen retrieval, and rinsed with PBS. Nonspecific antibody binding was blocked by incubating the sections for 10 min in Protein Block Serum-Free (X0909, DAKO, Glostrup, Denmark). Blocked sections were incubated for 1 h with anti-collagen I (ab292, Abcam, Cambridge, UK) or anti-elastin (PR533, Elastin Products Company, MO, USA) in 1% BSA/PBS. The sections were then rinsed four times with PBS and incubated for 1 h with Fluorescein(FITC)-conjugated goat anti-rabbit IgG (111-095-144) or Cy3-conjugated goat anti-rabbit IgG (111-165-144, Jackson ImmunoResearch Laboratories, PA, USA). The slides were then sealed using SlowFade Antifade Kit (S-2828, Molecular Probes, OR, USA). The slides were examined by a laser scanning confocal microscope (Carl Zeiss LSM510, Jena, Germany).
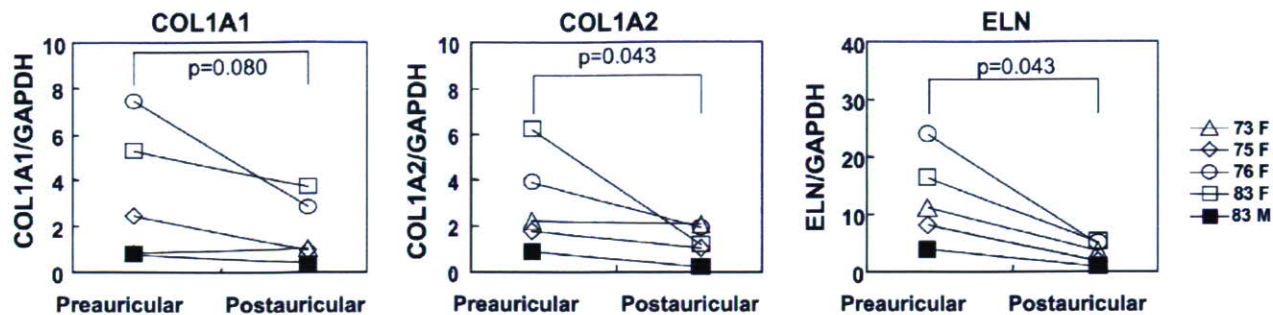
Fig. 2 Gene expression of procollagen and tropoelastin in the postauricular and preauricular skin. Total RNA were extracted from the postauricular and preauricular skin of the same subjects (n = 5), and applied to quantitative real-time PCR. Symbols shows age and sex of each subject. COL1A1, Type I collagen α1 subunit; COL1A2, Type I collagen α2 subunit; ELN, tropoelastin; GAPDG, glyceraldehydes-3-phosphate dehydrogenase
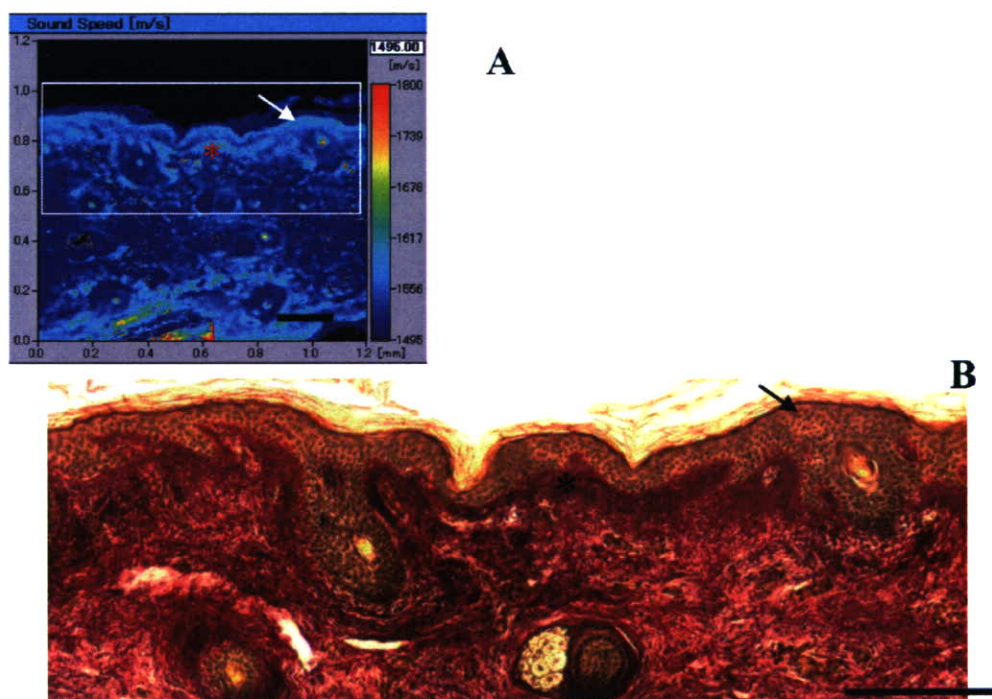

Fig. 3 Two-dimensional distribution of ultrasonic velocity and EVG staining of postauricular skin (66 year-old female). **A**, ultrasonic velocity; **B**, EVG stain. Higher ultrasonic velocity was observed in the uppermost of the stratum granulosum (arrow) and collagen layer beneath the epidermis (*).

RESULTS

To confirm the status of photodamage of aged preauricular skin, elastin and procollagen mRNA were measured by real-time PCR. The mRNA level of elastin in the preauricular skin was markedly increased compared with the postauricular skin (Fig. 2). Contrary to our expectations, the mRNA level of collagen α2 (I) in the preauricular skin was significantly increased and the mRNA level of collagen α1 (I) in the preauricular

skin also tend to be increased, compared with the postauricular skin.

Figure 3 shows EVG staining and the acoustic image of postauricular skin (photo-protected area) of a female (66 years old). The sound speed varied from about 1500 to 1600 m/s in the tissue. The uppermost layer of keratinocytes and the dermis beneath the epidermis showed a relatively higher sound speed (light blue). The uppermost layer of keratinocytes seemed to coincide with the granular layer in the epidermis. The collagen
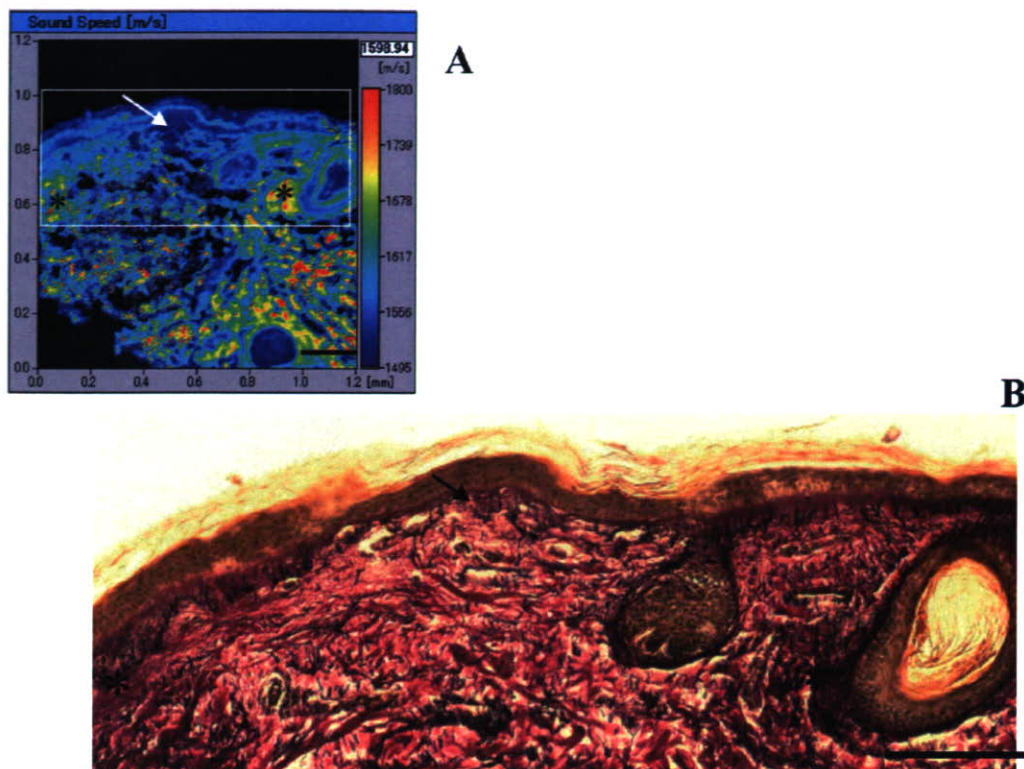
Fig. 4 Two-dimensional distribution of ultrasonic velocity and EVG staining of buttock skin. **A**, ultrasonic velocity; **B**, EVG stain. Decreased ultrasonic velocity was observed in the thin collagen layer beneath the epidermis (arrow). Higher ultrasonic velocity was observed in the dunning thick collagen fibers in the deeper dermis (✻). Scale, 200µm
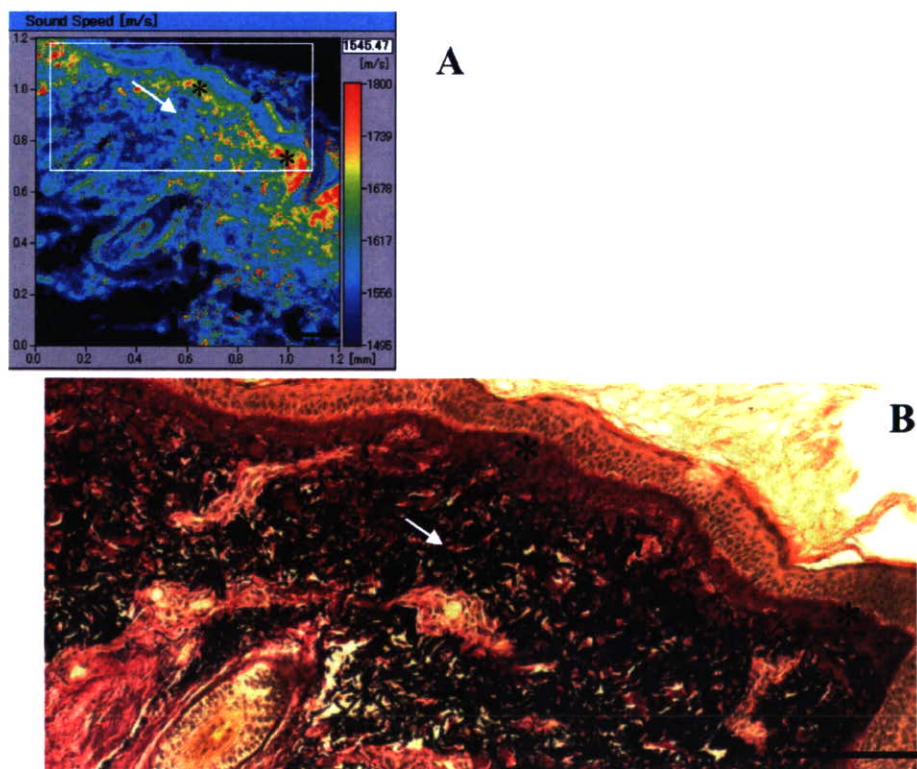

Fig. 5 Two-dimensional distribution of ultrasonic velocity and EVG staining of preauricular skin of subject shown in Fig. 3. **A**, ultrasonic velocity; **B**, EVG stain. Increased ultrasonic velocity in the Grenz zone (✻) and decreased ultrasonic velocity in the solar elastosis were observed (arrow). Scale, 200µm
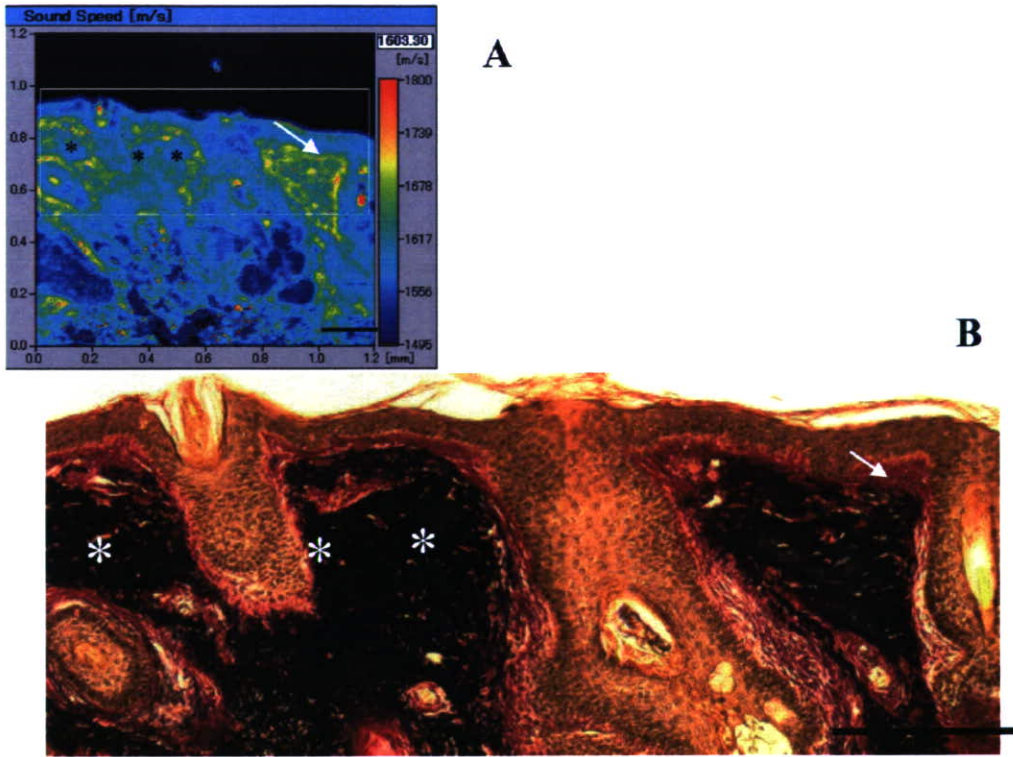
Fig. 6 Two-dimensional distribution of ultrasonic velocity and EVG staining of preauricular skin (69 year-old male). **A**, ultrasonic velocity; **B**, EVG stain. Increased ultrasonic velocity in the Grenz zone (arrow) and decreased ultrasonic velocity in part of the solar elastosis were observed (*). Scale, 200μm
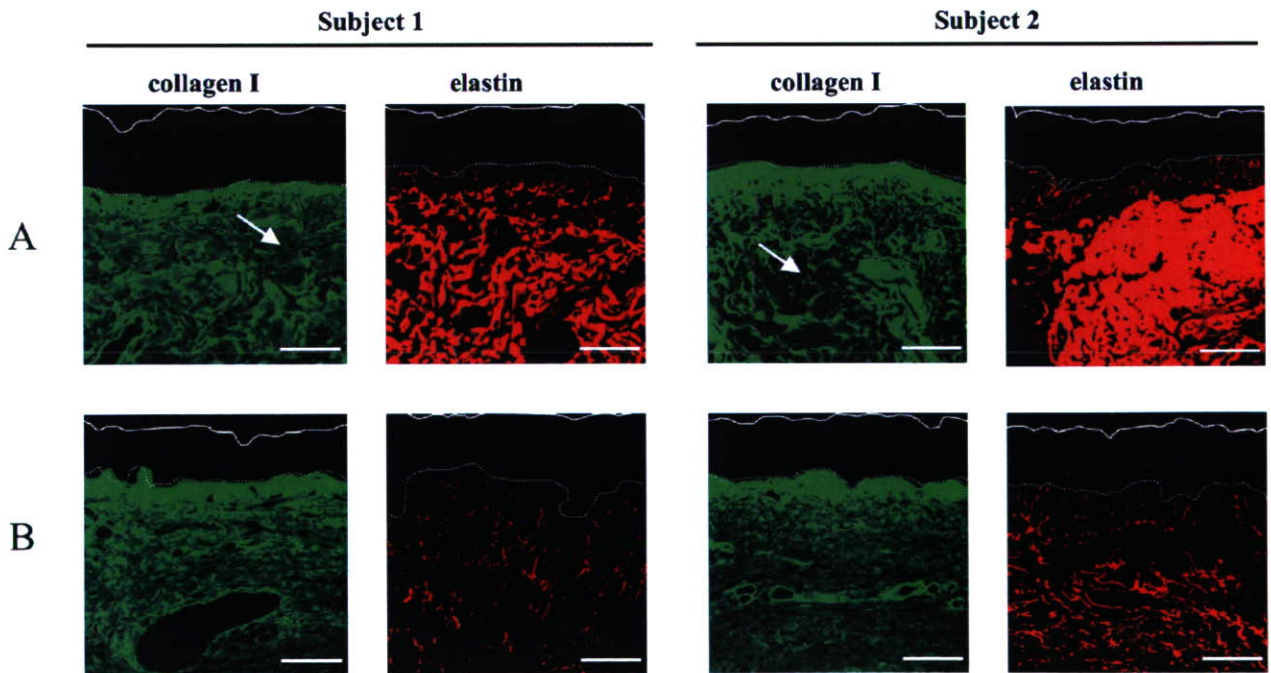

Fig. 7 Protein expression of procollagen and tropoelastin in postauricular and auricular skin. Preauricular (**A**) and postauricular skin (**B**) was obtained from subject 1 (shown in Fig. 3 and 5) and subject 2 (shown in Fig. 6). Procollagen (green) and tropoelastin (red) were stained immunohistochemically using corresponding antibodies. The dashed line shows the dermo-epidermal junction. The solid line shows the surface of the skin. Decreased signal (arrow) was observed at the site of solar elastosis. Scale, 100μm.

layer in the dermis beneath the epidermis had hardly any anchoring structure of oxytalan fibers as seen in the buttock skin (Fig. 3) but maintained an sound speed of about 1600 m/s, suggesting that the collagen layer sustained the physical strength of tissue. Figure 4 shows images of buttock skin (photo-protected area) of a female (69 years old). A decrease in sound speed was observed in the thin collagen layer without a progressive anchoring structure of oxytalan fibers. In the deeper dermis, higher sound speed (more than 1700 m/s) was observed in the thicker collagen fiber.

Figure 5 shows images of preauricular skin (photodamaged area) of a female (66 years old). The Grenz zone, which is a hallmark of photodamage, was developed on a clump of degenerated thick elastic fibers. The Grenz zone showed a higher sound speed (more than 1700 m/s). A decrease in the sound speed in part of the solar elastosis was observed. In the other case of preauricular skin (Fig. 6, 69 year-old male), solar elastosis was highly developed and the Grenz zone could be distinguished clearly by the sound speed (yellow to red).

To investigate the collagen content in the Grenz zone, skin samples were immunohistochemically stained using the antibody for collagen I. This antibody showed a stronger signal in the papillary dermis than in the deeper dermis both in the preauricular and postauricular skin (Fig. 7). The Grenz zone was clearly distinguished from the site of the deposition of elastin as seen by EVG staining in the preauricular skin. The Grenz zone conserved the signal of collagen I even in the more photodamaged preauricular skin (Fig. 7, subject 2). Deeper dermis showed a decreased signal of collagen I in part of the solar elastosis site.

DISCUSSION

In the present study, we first demonstrated the two-dimensional sound speed images of skin tissue at the microscopic level using scanning acoustic microscopy. We found four characteristic properties of sound speed in the skin as follows; (1) high sound speed of the keratinizing layer in the uppermost layer of the stratum granulosum, (2) discontinuous distribution of sound speed in the collagen layer beneath the epidermis in aged skin, (3) high sound speed associated with thick collagen fibers in the deeper dermis, and (4) an increase in the sound speed in the Grenz zone in photodamaged skin.

On the assumption that biological tissue is fluid-like, the sound speed is considered to be:

$$C = \sqrt{(K/\rho)} \qquad (7).$$

where C is the sound speed, K is the elastic bulk modulus and ρ is the density. High molecular mass and highly elastic components in the skin increase the sound speed. Saijo et al. reported high sound speed associated with stiffness in fibrotic sites in the tissue of the infarcted myocardium. The sound speed is considered depend on the content and quality of collagen fibers [11]. In fact the intensity (dark pink color) of the EVG stain is almost coincident to with the sound speed in this study. Increased sound speed was associated with thicker collagen fiber in the deeper dermis of buttock skin.

The sound speed of the keratinizing layer on the uppermost layer of the stratum granulosum may reflect the condition of differentiation of keratinocytes because keratinocytes produce and cross-link with keratin and components of the cornified envelope in the terminal differentiation to corneocytes to produce rigid stratum corneum [13]. Cross-linking of the cornified envelope may be a polymerizing process influencing the sound speed. A discontinuous layer of sound speed is sometimes observed in the skin, suggesting the heterogeneous keratinizing state of the stratum corneum on the surface of the skin.

We choose postauricular skin as photo-protected skin. We confirmed markedly extremely increased expression of elastin gene in the preauricular skin, compared with the postauricular skin. Generally, buttock or forearm skin is often used as photo-protected skin in the study of photoaging. but there are few reports demonstrating a comparison between postauricular skin and preauricular skin. Bhawan et al. pointed structural differences between facial skin and forearm skin as photodamaged skin [1, 12]. When compared with buttock skin, postauricular skin has some differences as follows; (1) less anchoring structure of oxytalan fibers beneath the epidermis, (2) low content of elastic fibers and (3) a decrease in the sound speed in the dermis, suggesting that there

is a difference not only in the structure but also in physical properties. Disappearance of the anchoring structure of oxytalan fibers beneath the epidermis and decreased content of elastic fibers are the main changes in intrinsically aged skin [14]. The postauricular skin is reasonable as photo-protected skin compared with buttock skin.

Interestingly, in the postauricular skin, the papillary dermis showed a higher sound speed than that of deeper dermis. This zone is considered to be a site where newly synthesized collagen is localized [15, 16]. We also confirmed an intensive immunochemical signal of collagen I in the papillary dermis in the postauricular skin. This zone may have an important role in sustaining the strength of the skin. Alternately, the decrease in the sound speed was observed in the thin collagen layer without an anchoring structure of oxytalan fibers in the buttock skin, suggesting that the progression of oxytalan fiber may be related to the synthesis of collagen and the strength of collagen fibers.

Photodamaged skin shows hallmarks such Grenz zone formation and solar elastosis [17], but the physiological function of this zone has been not clarified. We first found that the Grenz zone showed a higher sound speed more than the site of solar elastosis, and that the sound speed in part of the solar elastosis was actually decreased. Moreover, we detected deposition of collagen I in the Grenz zone even in the more photodamaged preauricular skin. These results suggest that the fibrosis in the Grenz zone compensates the strength of tissue with the progress of solar elastosis. Photoaging brings a decreased elasticity of the skin. Ultraviolet rays are considered to promote the decrease in the collagen content [2], degeneration of collagen fibers [3], and accumulation of degenerated elastin [18]. In the Grenz zone, type I collagen synthesis is considered to be depressed in photodamaged skin [2, 16] and degenerated collagen fibers are observed [19, 20]. Type VII collagen synthesis is also reported to be depressed [21], although some reports demonstrate that the synthesis of type I collagen [22], type III collagen [23] and type VI collagen [24] is maintained in the Grenz zone. These discrepancies may be due to the status of photodamage and/or the examined site. We detected overall increased expression of collagen gene and conserved

deposition of collagen I in the Grenz zone in the preauricular skin. Chung et al. also reported an increase in the collagen mRNA level in photoaged skin [22]. They argued that the degradation of collagen by MMPs was activated in the photodamaged skin. But localized modification of collagen may also take place in photodamaged skin. At least, the Grenz zone seems to exhibit different collagen metabolism than the the deeper dermis in photodamaged skin. Lavker emphasized that the Grenz zone, which had packed collagen fibrils in colinear arrangement, was a fibrosis-like microscar [17]. The Grenz zone may not be simply damaged, and rather plays an important role in sustaining the physical strength of photodamaged skin by rescuer fibrosis.

In conclusion, this study is the first to demonstrate the change of heterogeneous physical strength in the photodamaged skin using the SAM system. The SAM system will did in clarification of the role of structural proteins in photodamaged skin.

REFERENCES

1) Bhawan J, Andersen W, Lee J, Labadie R, Solares G. Photoaging versus intrinsic aging: a morphologic assessment of facial skin. J Cutan Pathol 1995; 22(2): 154-9.

2) Talwar HS, Griffiths CE, Fisher GJ, Hamilton TA, Voorhees JJ. Reduced type I and type III procollagens in photodamaged adult human skin. J Invest Dermatol 1995; 105(2): 285-90.

3) Nishimori Y, Edwards C, Pearse A, Matsumoto K, Kawai M, Marks R. Degenerative alterations of dermal collagen fiber bundles in photodamaged human skin and UV-irradiated hairless mouse skin: possible effect on decreasing skin mechanical properties and appearance of wrinkles. J Invest Dermatol 2001; 117(6): 1458-63.

4) Imokawa G, Takema Y, Yorimoto Y, Tsukahara K, Kawai M, Imayama S. Degree of ultraviolet-induced tortuosity of elastic fibers in rat skin is age dependent. J Invest Dermatol 1995; 105(2): 254-8.

5) Inomata S, Matsunaga Y, Amano S, Takada K, Kobayashi K, Tsunenaga M, et al. Possible involvement of gelatinases in basement membrane damage and wrinkle formation in chronically ultraviolet B-exposed hairless mouse. J Invest Dermatol 2003; 120(1): 128-34.

6) Cua AB, Wilhelm KP, Maibach HI. Elastic properties of human skin: relation to age, sex, and anatomical region. Arch Dermatol Res 1990; 282(5): 283-8.

7) Holbrook KA, Byers PH. Skin is a window on heritable disorders of connective tissue. Am J Med Genet 1989; 34(1): 105-21.

8) Ushiki T. Collagen fibers, reticular fibers and elastic fibers. A comprehensive understanding from a

morphological viewpoint. Arch Histol Cytol 2002; 65(2): 109-26.

9) Verdonk ED, Wickline SA, Miller JG. Anisotropy of ultrasonic velocity and elastic properties in normal human myocardium. J Acoust Soc Am 1992; 92(6): 3039-50.

10) Hoffmeister BK, Verdonk ED, Wickline SA, Miller JG. Effect of collagen on the anisotropy of quasi-longitudinal mode ultrasonic velocity in fibrous soft tissues: a comparison of fixed tendon and fixed myocardium. J Acoust Soc Am 1994; 96(4): 1957-64.

11) Saijo Y, Sasaki H, Naganuma T, Tanaka M. Ultrasonic tissue characterization of diseased myocardium by scanning acoustic microscopy. J Cardiol 1995; 25(3): 127-32.

12) Bhawan J, Oh CH, Lew R, Nehal KS, Labadie RR, Tsay A, et al. Histopathologic differences in the photoaging process in facial versus arm skin. Am J Dermatopathol 1992; 14(3): 224-30.

13) Nemes Z, Steinert PM. Bricks and mortar of the epidermal barrier. Exp Mol Med 1999; 31(1): 5-19.

14) Kligman AM, Zheng P, Lavker RM. The anatomy and pathogenesis of wrinkles. Br J Dermatol 1985; 113(1): 37-42.

15) Kligman LH. Effects of all-trans-retinoic acid on the dermis of hairless mice. J Am Acad Dermatol 1986; 15(4 Pt 2): 779-85, 884-7.

16) Nelson BR, Majmudar G, Griffiths CE, Gillard MO, Dixon AE, Tavakkol A, et al. Clinical improvement following dermabrasion of photoaged skin correlates with synthesis of collagen I. Arch Dermatol 1994; 130(9): 1136-42.

17) Lavker RM. Structural alterations in exposed and unexposed aged skin. J Invest Dermatol 1979; 73(1): 59-66.

18) Bernstein EF, Chen YQ, Tamai K, Shepley KJ, Resnik KS, Zhang H, et al. Enhanced elastin and fibrillin gene expression in chronically photodamaged skin. J Invest Dermatol 1994; 103(2): 182-6.

19) Bernstein EF, Chen YQ, Kopp JB, Fisher L, Brown DB, Hahn PJ, et al. Long-term sun exposure alters the collagen of the papillary dermis. Comparison of sun-protected and photoaged skin by northern analysis, immunohistochemical staining, and confocal laser scanning microscopy. J Am Acad Dermatol 1996; 34(2 Pt 1): 209-18.

20) Yamamoto O, Bhawan J, Solares G, Tsay AW, Gilchrest BA. Ultrastructural effects of topical tretinoin on dermo-epidermal junction and papillary dermis in photodamaged skin. A controlled study. Exp Dermatol 1995; 4(3): 146-54.

21) Craven NM, Watson RE, Jones CJ, Shuttleworth CA, Kielty CM, Griffiths CE. Clinical features of photodamaged human skin are associated with a reduction in collagen VII. Br J Dermatol 1997; 137(3): 344-50.

22) Chung JH, Seo JY, Choi HR, Lee MK, Youn CS, Rhie G, et al. Modulation of skin collagen metabolism in aged and photoaged human skin in vivo. J Invest Dermatol 2001; 117(5): 1218-24.

23) El-Domyati M, Attia S, Saleh F, Brown D, Birk DE, Gasparro F, et al. Intrinsic aging vs. photoaging: a comparative histopathological, immunohistochemical, and ultrastructural study of skin. Exp Dermatol 2002; 11(5): 398-405.

24) Watson RE, Ball SG, Craven NM, Boorsma J, East CL, Shuttleworth CA, et al. Distribution and expression of type VI collagen in photoaged skin. Br J Dermatol 2001; 144(4): 751-9.

ACOUSTIC MICROSCOPY BASED ON FREQUENCY DOMAIN ANALYSIS OF A SINGLE PULSED WAVE

Y. Saijo*, N. Hozumi**, K. Kobayashi***, N. Okada***, K. Fukuma****,
N. Tanaka*****, H. Sasaki*, M. Tanaka*, and T. Yambe*

* Department of Medical Engineering and Cardiology, Institute of Development, Aging and Cancer,
Tohoku University, Sendai, Japan
** Toyohashi University of Technology, Toyohashi, Japan
*** Honda Electronics Co. Ltd., Toyohashi, Japan
**** TrafficSim Co. Ltd., Nagoya, Japan
***** Shibaura Institute of Technology, Omiya, Japan

E-Mail Address: saijo@idac.tohoku.ac.jp

Abstract: Scanning acoustic microscopy (SAM) for biomedicine is useful for intra-operative pathological examination, understanding of lower frequency ultrasonic images, and assessment of biomechanics at a microscopic level. Recently, we have proposed a new concept SAM utilizing a single pulsed wave instead of continuous waves used in conventional SAM systems. Speed of sound images of 300x300 pixels were successfully obtained within 150 sec.

Introduction

Since 1985, we have been developing a scanning acoustic microscope (SAM) system for biomedical use and have been investigating acoustic properties of various organs and various disease states with this SAM system [1-2]. SAM for biomedicine is useful for intra-operative pathological examination, understanding of lower frequency ultrasonic images, and assessment of biomechanics at a microscopic level. The originality of our traditional SAM system is that it can provide quantitative values of attenuation and sound speed of a thinly sliced soft tissue.

Recently, we have proposed a new concept SAM utilizing a single pulsed wave instead of continuous waves used in conventional SAM systems [3]. Here, we present example images of some kinds of pathological specimens.

Materials and Methods

System: Figure 1 shows a block diagram of sound speed microscopy for biological tissue characterization. A single pulsed ultrasound with 5 ns pulse width was emitted and received by the same transducer above the specimen. The aperture diameter of the transducer was 1.2 mm and the focal length was 1.5 mm. The central frequency was 80 MHz and the pulse repetition rate was 10 kHz. Considering focal distance and the sectional area of the transducer, the diameter of focal spot was estimated as 20 micron at 80 MHz. Distilled water was used as the coupling medium between the transducer and the specimen. The reflections from the tissue surface and from the interface between tissue and glass were received by the transducer and were introduced into a digital oscilloscope (Tektronics TDS 5052, USA). The frequency range was 300 MHz and the sampling rate was 2.5 GS/s. Four times of pulse responses at the same point were averaged in the oscilloscope in order to reduce random noise.

The transducer was mounted on an X-Y stage with a microcomputer board which was driven by the computer installed in the digital oscilloscope through RS-232C. X-scan was driven by a linear servo-motor and Y-scan was driven by a stepping motor. Finally, two-dimensional distributions of ultrasonic intensity, sound speed and thickness of the specimen of 2.4 by 2.4 mm area were visualized with 300 by 300 pixels. Total scanning time was 150 sec.
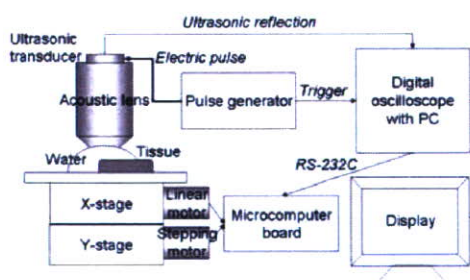

Figure 1: Block diagram of the system

Signal Analysis: The reflected wave at the glass surface without tissue was employed as a reference waveform. The wave from the tissue area contained two reflections at the surface and the interface of tissue and glass. The frequency domain analysis was performed by analyzing interference between two components which cannot be separated in time domain analysis. Intensity and phase spectra were calculated by Fourier-transforming the waveform. The spectra were

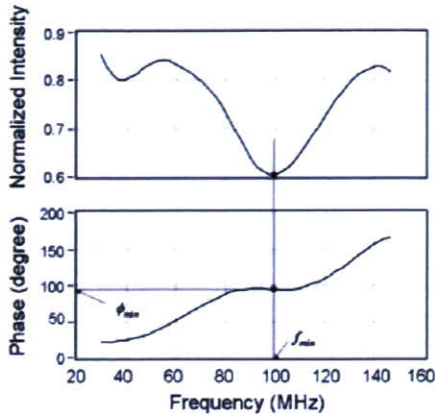normalized by the reference waveform. Figure 2 shows the frequency domain analysis of interfered waves.

Figure 2: Frequency domain analysis of interfered waves

Assuming f_{min} as the minimum point in the intensity spectrum, and ϕ_{min} as the corresponding phase angle, the phase difference between the two reflections at the minimum point is $(2n-1)\pi$, giving

$$2\pi f_{min} \times \frac{2d}{c_0} = \phi_{min} + (2n-1)\pi \cdots (1)$$

where d, c_0, and n are the tissue thickness, sound speed of the water, and a non-negative integer, respectively. The phase angle ϕ_{min} can be expressed by

$$2\pi f_{min} \times 2d\left(\frac{1}{c_0} - \frac{1}{c}\right) = \phi_{min} \cdots (2)$$

since ϕ_{min} is the phase difference between the wave passed through the distance $2d$ with sound speed c and that passed through the corresponding distance with sound speed c_0. By solving the equations (1) and (2),

$$d = \frac{c_0}{4\pi f_{min}}\left\{\phi_{min} + (2n-1)\pi\right\} \cdots (3)$$

is obtained. Speed of sound at the minimum point frequency is finally calculated as

$$c = \left(\frac{1}{c_0} - \frac{\phi_{min}}{4\pi f_{min}d}\right) \cdots (4)$$

Results

Figure 3 is a snapshot of the PC window showing a SAM image. The upper left is the intensity image, the upper middle is the speed of sound image, the upper right is the waveform, and the lower middle is the thickness image, respectively. The example is breast cancer with scirrhous change. The speed of sound is 1700 m/s at the fibrotic lesion while that is 1560 m/s in the ductus area.
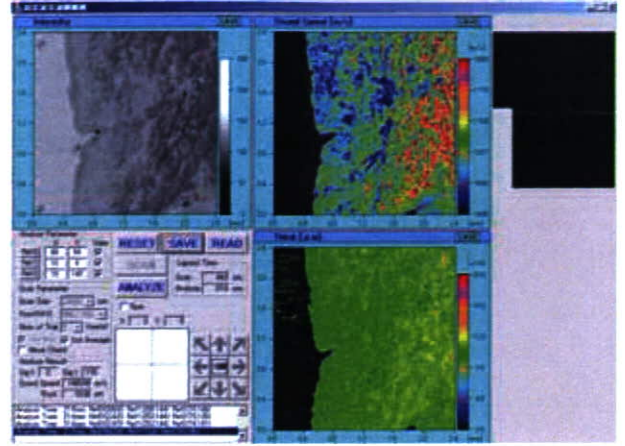

Figure 3: A snapshot of the PC window showing a SAM image

Discussion

The speed of sound image obtained with the new concept SAM showed physical characteristics of breast cancer with scirrhous change. Fibrotic lesion showed higher speed of sound than normal breast ductus area. The data acquisition of one frame was 8sec in conventional SAM and 150 sec in speed of sound SAM. However, the operator of conventional SAM required a skill, for example, to correct tilting of specimen. The correction of tilting was done automatically in sound speed microscopy and the user interface was friendly to medical and pathological researcher.

Conclusions

An acoustic microscope system which can measure sound speed of thinly sliced biological material was developed. It was a unique acoustic microscope because it used a single pulse and Fourier transform to calculate sound speed at all the measuring points. Although the data acquisition time of one frame was longer than the conventional SAM, total time for calculation was significantly shorter. It can be applied to intra-operative pathological examination.

References

[1] SAIJO Y, TANAKA M, OKAWAI H, SASAKI H, NITTA S, DUNN F (1997) 'Ultrasonic tissue characterization of infarcted myocardium by scanning acoustic microscopy', *Ultrasound Med Biol* **23** pp. 77-85.

[2] SAIJO Y, MIYAKAWA T, SASAKI H, TANAKA M, NITTA S (2004) 'Acoustic properties of aortic aneurysm obtained with scanning acoustic microscopy', *Ultrasonics* **42** pp. 695-698.

[3] HOZUMI N, YAMASHITA R, LEE CK, NAGAO M, KOBAYASHI K, SAIJO Y, TANAKA M, TANAKA N, OHTSUKI S (2004) 'Time-frequency analysis for pulse driven ultrasonic microscopy for biological tissue characterization', *Ultrasonics* **42** pp. 717-722.

FULLY-AUTOMATIC MEASUREMENT OF FLOW MEDIATED DILATATION

Y. Saijo*, Y. Akino**, S. Watanabe**, K. Oba***,
K. Tamamura***, Y. Yamazaki***, and T. Ishiguro****

* Department of Medical Engineering and Cardiology, Institute of Development, Aging and Cancer,
Tohoku University, Sendai, Japan
** Miyagi Social Insurance Hospital, Sendai, Japan
*** Fukuda Denshi Co. Ltd., Tokyo, Japan
**** Chunichi Denshi Co. Ltd., Nagoya, Japan

E-Mail Address: saijo@idac.tohoku.ac.jp

Abstract: Flow mediated dilatation (FMD) is a clinically available, important parameter of vascular endothelial function. However, the measurement of FMD was difficult because skilful and precise measurement based on B-mode ultrasound was required. We propose a novel measuring system of FMD based on change of vascular compliance by analyzing pulsed wave pressure and volume. FMD was successfully obtained in healthy volunteers but the time course was different from that obtained by conventional ultrasound measurement.

Introduction

Flow mediated dilatation (FMD) is a clinically available parameter of vascular endothelial function. FMD is reactive hyperemia caused by releasing nitric oxide (NO) from vascular endothelium after occluding and releasing brachial artery. FMD is a good predictive factor of atherosclerosis and is very sensitive to drug response [1-3]. Previously, FMD has been measured by B-mode ultrasound [4]. However, the measurement required skilful sonographers and the precision of measurement was limited by the frequency of ultrasound.

In the present study, we propose a novel measuring algorithm of FMD based on beat by beat calculation of vascular compliance by analyzing pulsed wave pressure and volume simultaneously.

Materials and Methods

Subjects: Ten healthy volunteers (18-62 years old, male) were involved. Smoking or eating was prohibited before 30 minutes of measurement. Written informed consent was obtained from each volunteer.

Electrocardiogram (ECG): Electrocardiogram was monitored during measurement by conventional electrodes.

Pulsed Wave Volume: Pulsed wave volume was measured by electrical impedance change of the forearm. Two sheet electrodes were attached 10 cm apart on the forearm and electric impedance was measured.

Pulsed Wave Pressure: Pulsed wave pressure was measured by a ceramic piezoelectric sensor attached upon the radial artery.

B-mode Ultrasound: The diameter of brachial artery was measured by conventional B-mode ultrasound with central frequency of 13-MHz as a reference. The probe was fixed upon the brachial artery by a special probe holder.

Experimental Setup: The volunteer was laid on a bed in dark condition with adequate air-conditioning. Blood pressure (BP) was measured and the brachial artery was occluded by a cuff at the pressure 50 mmHg higher than the systolic BP. All the parameters (electrocardiogram, pulsed wave pressure, pulsed wave volume and ultrasound) were recorded before occlusion as control. The occlusion was maintained for 5 minutes. All the parameters were again recorded beat by beat until 15 minutes after occluding brachial artery. Figure 1 shows the experimental setup.
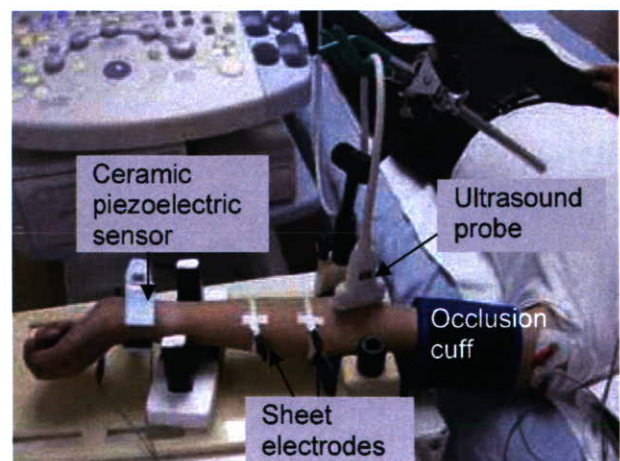

Figure 1: The Experimental Setup

Calculation of FMD: As the vascular compliance can be calculated by equation (1).

$$C = \frac{\Delta V}{\Delta P} = \frac{2\pi R^3 (1-\sigma^2)}{Eh} \cdots (1)$$

The radius of the artery can be expressed as equation (2),